Thrust enhancement due to flexible trailing-edge of plunging foils

D.J. Cleaver, I. Gursul, D.E. Calderon, Z. Wang

Department of Mechanical Engineering, University of Bath, Bath, BA2 7AY, UK

Abstract

Drag reduction for hydrofoils is studied through thrust generation on plunging foils in order to simulate the action of the ocean waves. Force, deformation and flow field measurements are presented for a partially flexible plunging foil in water tunnel experiments. The foil is predominantly rigid with a short flexible trailing-edge plate of length: L = 0.1c, 0.2c, or 0.3c. Appropriate flexibility increases thrust compared to the rigid case. Flexibility is generally more effective for larger lengths of the flexible plate and smaller plunge amplitudes. The maximum observed is therefore for the largest length and smallest amplitude studied: L = 0.3c and a = 0.1c and equates to 28% more thrust than the rigid case. Optima are observed in the non-dimensional rigidity (λ) versus flap angle amplitude (δ) parameter space. These occur at $\lambda \approx 2$ and $\delta \approx 7^0$ to 13^0 for a wide range of flexible plate length and plunge amplitude. Whilst a satisfactory explanation of why there is an optimal flap amplitude remains unavailable, the case of optimal flap angle amplitude results in increased trailing-edge vortex circulation, giving a stronger reverse Kármán vortex street and thus a stronger time-averaged jet.

Nomenclature

a	plunge amplitude
A	peak-to-peak amplitude ($2a$)
A_w	wave amplitude
c	chord length
C_d	time-averaged drag coefficient
C_{d0}	time-averaged drag coefficient for stationary foil
E	Young's modulus
f	plunge frequency
I	area moment of inertia
k	reduced frequency (πSr_c)
L	length of the flexible plate
Re	Reynolds number
s	thickness of the plate
Sr_A	Strouhal number based on the amplitude
Sr_c	Strouhal number based on the chord length
U_∞	free stream velocity
α	angle of attack
α_{eff}	maximum effective angle of attack
Γ	circulation
δ	flap angle
λ	aeroelastic parameter
λ_w	wavelength of the ocean waves

1. Introduction

It is well established that the drag force for a foil can be reduced through plunging oscillations; indeed given large enough plunge velocities this motion can even create thrust. Research for thrust generation from plunging airfoils and wings has traditionally been focused towards micro air vehicle and aquatic propulsion applications. However, there are also possible applications for hydrofoils (Cleaver et al., 2013). The concept is that any hydrofoil moving near an undulating free surface will be subject to an oscillatory freestream that is comparable to a foil oscillating in a steady freestream. It is therefore possible to exploit the unsteady freestream as a means of drag reduction. For hydrofoils the degree of relative motion is crucial and will depend on both the flow within the wave and the response of the craft to the wave. There is an infinite range of possible velocity waveforms so for simplicity it can be assumed to be sinusoidal with the maximum plunge amplitude possible being the amplitude of the free surface. This can be taken to be the value of a Stokes ideal wave (Michell, 1893; Tsuji and Nagata, 1973): amplitude-to-wavelength ratio A_w/λ_w = 1/7 which, assuming that the wave velocity is small compared to the craft velocity, equates to a non-dimensional plunge velocity of $Sr_A = fA/U_\infty = 2fa/U_\infty = 0.142$. This represents a theoretical maximum that will not be surpassed. Alternatively a value that can be taken to be indicative of the average is derived from the Pierson-Moskowitz sea spectrum (Pierson and Moskowitz, 1964): $Sr_A = 0.076$. This value is independent of vessel speed, hydrofoil chord length and sea state. Therefore we focus on different kinematics (plunge amplitude and frequency) to past work where the main interest is biologically inspired flows which have much larger amplitudes and frequencies. Cleaver et al. (2013) demonstrated that if exploited the amount of drag reduction can be significant as long as the frequencies associated with an unsteady parameter of $\tau = 2\pi fU_\infty/g = 0.25$ are avoided. Around this value of unsteady parameter there are significant drag-increasing foil-wave interactions (Cleaver et al., 2013; Palm and Grue, 1999; Zhu et al., 2006).

In addition it has previously been shown that the propulsive performance of an oscillating foil can be further enhanced through the application of appropriate chordwise flexibility. For example, a flexible foil made of a small rigid leading-edge and a long flexible aft section (length $L = 2c/3$) can increase mean thrust significantly (Heathcote and Gursul, 2007). Likewise, it was found that a flexible foil with a pre-defined deformation can increase propulsive efficiency (Miao and Ho, 2006). The effects of chordwise and spanwise flexibility (Heathcote et al., 2008) on thrust and propulsive efficiency are discussed in more detail in a

recent review article (Gursul et al., 2013). The primary objective of this study is to investigate if the thrust augmenting effect of flexibility can still be realized in the case of a foil with the flexibility confined to a small section near the trailing-edge in the form of a short thin plate (see Fig. 1) undergoing a plunging motion. This geometry is considered to be more practical if the flexibility is to be exploited for drag reduction of hydrofoils. Also, the main focus in this paper will be the time-averaged drag/thrust as the propulsive efficiency is not considered to be essential for hydrofoils plunging *passively* due to surface waves, because the waves provide the input power required for the plunging motion. Therefore we aim to maximize time-averaged thrust.

The inviscid simulations of Michelin and Smith (2009) suggest that for a given foil flexibility but varying plunge frequency, the maximum mean thrust is produced when the trailing-edge amplitude is maximum. In contrast the analysis of Kang et al. (2011) suggest that the relative, rather than absolute, deformation of the trailing-edge determines the mean thrust, and maximum propulsive force is obtained when plunging near the resonance. These viscous fluid-structure interaction simulations showed good agreement with the experiments of Heathcote and Gursul (2007). A somewhat different suggestion was put forward by Ramananarivo et al. (2011) based on the experiments on a self-propelled flapping wing with chordwise flexibility, mounted on a rotating arm. They suggest that the maximum thrust is obtained when the airfoil shape varies in a way to optimize the aerodynamics (minimize flow separation), rather than maximum trailing-edge amplitude. They propose that when the airfoil slope at the trailing-edge equals the maximum effective angle of attack, the airfoil is "tuned" and produces maximum thrust. Hence, there is some debate on when the maximum thrust is achieved. As discussed in the recent review article (Gursul et al., 2013), it is generally believed that this occurs near resonance.

To allow fair comparison the effect of flexibility (bending stiffness) is most interesting for a fixed plunge frequency and amplitude, i.e., the only variable is flexibility. For a given frequency-amplitude combination there is significant evidence for the existence of optimal flexibility, summarized in Gursul et al. (2013). For this optimal case stronger trailing-edge vortices form further apart giving a wider time-averaged jet. The maximum thrust, for a fixed plunge frequency, does not however correspond to the maximum relative deformation of the trailing-edge (see Figure 18a and 21a in Heathcote and Gursul, 2007). Hence there is a suggestion of optimal relative deformation. Therefore we consider the flap angle shown in Figure 2, which is a direct measure of the relative deformation. The second

objective of this study is to investigate this aspect: is there optimal flap amplitude, if the short flexible plate attached to the foil is considered to be a passive flap? In this article we are purely concerned with drag reduction / thrust generation and not efficiency because we consider hydrofoil applications where the vertical motion is passively created and power is therefore inconsequential.

2. Experimental Apparatus and Procedures

Force and Particle Image Velocimetry (PIV) measurements were conducted for a plunging NACA 0012 airfoil mounted horizontally in a closed-loop water channel, see Fig. 1 (a). For a review of parameters studied, see Table 1; all uncertainties are calculated based on the methods of Moffat (1988) taking into account both bias and precision errors. Note that Strouhal number is directly related to the reduced frequency through: $Sr_c = k/\pi$.

Table 1 Experimental Parameters

Parameter	Range Considered	Uncertainty
Re	40,000	+/- 200
α	0°	+/- 0.5°
a/c	0.1, 0.2, 0.5	+/- 0.003
c	0.1 m	+/- 0.0005 m
d/c	2.25	+/- 0.02
Fr	0.43	+/- 0.03
Sr_c	0 to 0.8	+/- 2.3%
Sr_A	0 to 0.16	+/- 0.0012
U_∞	0.43 m/s	+/- 0.005 m/s

2.1 Experimental Setup

The experiments were conducted in a free-surface closed-loop water channel (Eidetics Model 1520) at the University of Bath. The water channel is capable of flow speeds in the range 0 to 0.5 m/s and has a working section of dimensions 381 mm x 508 mm x 1530 mm. The turbulence intensity has previously (Heathcote, 2006) been measured by laser Doppler velocimetry to be less than 0.5%.

Mounted on top of the channel is the experimental rig, see Fig. 1 (a). This consists of a carriage mounted on New Way air bushings, which is driven by an Aerotech BLMC linear motor controlled by an Aerotech Soloist CP controller with position feedback from a Renishaw Signum optical encoder. This system was capable of achieving sinusoidal

oscillations of arbitrary amplitude and depth with a maximum recorded position error of < 30 μm. Attached to this carriage is the binocular force balance described below. The wing is attached to the force balance through two, 2 mm thick, streamlined stainless steel stings mounted at either end. The wings spanned the test section wall to wall with a 2 mm clearance so as to remove tip effects. The wing was constructed by selective laser sintering from glass filled polyamide.

At operating conditions the water channel had a depth of 0.45 m. All results presented herein are for oscillations around a mean depth of d/c = 2.25. This is therefore half way between the bottom of the water channel and the free surface. At this depth the free surface has no effect (Cleaver et al., 2013).

Three NACA 0012 airfoils with various flexible trailing-edge lengths are considered, see Fig. 1b. The total chord length of all cross sections was maintained at 100 mm. This meant it was necessary to adjust the chord length of the NACA sections to maintain 1.4 mm thickness at 90 mm (L = 0.1c), 80 mm (L = 0.2c), and 70 mm (L = 0.3c) from the leading-edge. The thickness therefore varies in a small range: t/c = 0.108 to 0.084. The only practical alternative method of maintaining the t/c ratio and having a flexible trailing-edge section is to truncate the airfoil which would have a greater effect. Varying the t/c ratio but maintaining the geometry was therefore deemed to be the best possible solution.

All wings were constructed by selective laser sintering from glass filled nylon. For the flexible trailing-edge part to practically achieve an acceptable range of rigidity four different materials in a wide range of thicknesses were used to give a choice of 21 possible rigidities (EI) over a very wide spread, see Table 2 and the inset in Fig. 1b. All stated values of EI are per unit span. The flexible part was secured in a 1 mm groove at the rear of the airfoil using symmetrically placed shim material and grub screws embedded in tapped inserts. These were filled, smoothed, and repainted each time.

Table 2 Properties of the flexible trailing-edge parts

Number of Plates	**Material**	**Young's Modulus, E (Nm^{-2})**	**Thickness, s (mm)**
6	Stainless Steel	205×10^9	0.025 to 1
1	Aluminium	69×10^9	0.025
7	Polyester	3.5×10^9	0.013 to 0.127
7	Vinyl	3.4×10^9	0.191 to 0.762

2.2 Force Measurements

The force in the streamwise direction was measured through a binocular strain gauge force balance (Frampton et al., 2002). Two force balances of differing rigidities were used so as to achieve the desired accuracy whilst minimizing flexibility. The signal from the strain gauges was amplified by a Wheatstone bridge circuit and sampled at either 2 kHz for 21,600 samples (stationary cases), or 360 per cycle for 60 cycles (dynamic cases). The forces were then calculated from the average voltage through linear calibration curves. The calibration curves consisted of thirteen points, and were performed daily before testing. Each data set was repeated at least once and then averaged. This force measurement technique has previously been validated (Cleaver et al., 2013). Herein we are concerned with the drag reduction. This is defined as $C_d - C_{d0}$ where C_d is the time-averaged drag coefficient for the dynamic case and C_{d0} is the time-averaged drag coefficient for the stationary foil. The uncertainty in drag reduction was calculated for every measurement. The uncertainty increased with increasing frequency, a typical peak value is ± 0.008.

2.3 PIV Measurements

The flow was seeded with 8 – 12 μm hollow glass spheres. The velocity field around the airfoil was measured using a TSI Inc. 2D-PIV system consisting of a dual ND:YAG 50 mJ pulsed laser, 2 MP Powerview Plus 12 bit CCD camera and TSI Model 610034 synchronizer. The laser was positioned behind to illuminate a mid-span streamwise plane with the camera positioned to the side as shown in Fig. 1a. The PIV images were analyzed using the software Insight 3G. A FFT correlator using interrogation windows of 32 x 32 pixels with 50% overlap was selected to generate a vector field of 99 x 73 vectors, approximately giving a 2 mm spatial resolution. The phase-averaged data is derived from 100 to 200 pairs of images as required; the time-averaged data is derived from 500 pairs of images. Measurements over the wake region and leading-edge region were performed separately. These were then merged in MATLAB through interpolation of the wake region data onto the leading-edge region grid using the trailing-edge as the common reference point. The circulation is estimated as explained in Cleaver et al. (2012): the vortex is located using a vortex identification algorithm with the search centered on the point of maximum absolute vorticity. The radius of the vortex is then determined by continually expanding from the

center, one spatial resolution unit at a time, until the increase in the magnitude of circulation is negative or small (<1 %). The circulation calculation itself is done using both line integral and vorticity surface methods. The agreement between the two methods was generally very good. All circulation results presented herein are derived from the average of the two.

2.4 Deformation measurements

The deformation of the flexible section was measured by painting the wing black with a thin white line at the centre span. The motion of this line was tracked using the PIV camera described above. The instantaneous flap angle, δ, was derived from the position of the tip of the flexible part and the trailing-edge of the airfoil, see Fig. 2a. In MATLAB a sine fit was then applied to define the amplitude and phase lead of the deformation, see Fig. 2b. Note that the relative deformation is $L \tan \delta$.

3. Results and Discussion

Shown in Fig. 3 is the reduction in drag coefficient for an airfoil with a flexible trailing-edge part of length $L = 0.2c$ for three plunge amplitudes a/c = 0.1, 0.2 and 0.5, and a wide range of flexibilities. The results for a/c = 0.1 (Fig. 3a) demonstrate the same parabolic trend as previously observed for a rigid NACA 0012 airfoil (Cleaver et al., 2013), however in this case the gradient is determined by the flexibility. It is noted that this applies to the small amplitudes and low frequencies studied here, which are characteristic of hydrofoil drag reduction. Initially, increasing flexibility relative to the rigid case (EI = 1.7 x 10^{1} Nm, denoted by solid lines and circles), results in increasing gradient and therefore increasing drag reduction, leading to an optimum at EI = 2.1 x 10^{-3} Nm (denoted by solid lines and right triangles). Further increase in flexibility beyond this optimum (denoted by dashed lines) results in decreasing performance. At a/c = 0.2 (Fig. 3b) there are similar trends however the overall effect is greatly diminished. Hence although there are still parabolic trends with the gradient determined by the flexibility culminating in an optimum flexibility (EI = 6.0 x 10^{-4} Nm), the difference between this optimum and the rigid case is proportionally smaller. For a/c = 0.5 (Fig. 3c) the general shape of the curves is significantly different, it has previously been shown (Cleaver et al., 2013) that the 'kink' around St_A = 0.08 is due to leading-edge vortex formation. Apart from this change the curves again follow the same qualitative trends but the effect of flexibility is now so greatly diminished that it is not possible to define an

optimum to within the bounds of experimental uncertainty. The reasons for decreasing effectiveness with increasing plunge amplitude will be discussed later in the paper.

This amplitude dependence can be demonstrated by considering the improvement due to flexibility. This is defined as: $(\Delta C_{dF} - \Delta C_{dR})/ \Delta C_{dR}$, where ΔC_{dF} is change in drag coefficient for the flexible airfoil and ΔC_{dR} is change in drag coefficient for the rigid counterpart. Figure 4 shows a comparison of performance improvement for the maximum Sr_A studied against elastic parameter:

$$\lambda = \frac{\frac{Es^3}{12}}{0.5\rho U_\infty^2 L^3}$$

Note the use of the length L of the flexible plate in this definition, rather than the total chord length. The elastic parameter can be considered as the ratio of the nondimensional rigidity to the fluid dynamic forces. Figure 4b is for the same case as shown in Fig. 3, $L = 0.2c$. It demonstrates that flexibility can be advantageous over a very wide range of flexibilities (note the log scale), with an optimum of $\lambda \approx 2$. We find it interesting that Dewey et al (2013) also found an optimal value for propulsive efficiency of $\lambda \approx 2$ in spite of the major differences in their cases (low aspect ratio panels, pitching motion, Strouhal number in the range of 0.25 to 0.35). Unlike our setup, the effect of the tip vortices is expected to be significant for low aspect ratio pitching panels.

In addition flexibility is more effective for smaller amplitude resulting in a peak effectiveness of 24% for $a/c = 0.1$. Note that although this curve is only for $Sr_A = 0.16$, due to the parabolic nature of the curves (see Fig. 3) it is reasonable to expect similar curves at lower Strouhal numbers. The largest Strouhal number was chosen purely to minimize the effect of experimental uncertainty.

Similar curves for $L = 0.1c$ and $0.3c$ are shown in Fig. 4a and Fig. 4c respectively. The smaller flexible length generates a smaller proportional improvement. Smaller plunge amplitude is again more effective and both plunge amplitudes exhibit an optimum although this time in the region of $\lambda \approx 0.5$. The larger flexible length creates larger improvement, see Fig. 4c. It is again more effective at smaller amplitude leading to a peak improvement of 28% for $a/c = 0.1$. The optimum for this larger flexible part is in the region of $\lambda \approx 3$. We believe that there is no limit for the length of the flexible portion of the foil for enhanced propulsion, and therefore an entirely flexible foil would be ideal in order to maximize thrust (or drag reduction). This is demonstrated by the increasing performance improvement with length,

from around 8% for $L = 0.1c$, to 28% for $L = 0.3c$, up to 154% for $L = 2c/3$ (derived from Heathcote and Gursul 2007). However, such a hydrofoil would not be ideal for lift generation.

To understand how flexibility improves drag reduction, detailed deformation measurements were performed for a wide range of flexibilities and Strouhal numbers and in addition the flow fields for three flexibilities (from $L = 0.2c$ and $a/c = 0.1$) were studied through PIV measurements. These three PIV cases are labeled rigid, optimal, and post-optimal in Fig. 4b. Examples of the absolute and relative deformation measurements for $L = 0.2c$ and $a = 0.1c$, $0.5c$ are shown in Fig. 5 as a function of the Strouhal number based on the chord length. It is seen that for $a = 0.1c$, both the absolute amplitude and flap angle increase monotonically with Strouhal number. The maximum flap angle for the optimal case ($EI = 2.1\text{x}10^{-3}$ Nm, denoted by solid lines and right triangle) reaches $\delta = 7°$. For the post-optimal case ($EI = 1.3\text{x}10^{-4}$ Nm) the gradient is steeper resulting in a greater maximum flap angle around 20°. It is clear that both the absolute and relative deformation amplitude vary monotonically with elastic parameter. Also, the optimal flexible plate, which produces the largest thrust (maximum drag reduction) (shown with solid right triangle symbols and solid line) does not have the maximum amplitude of the absolute deformation, nor does it have the maximum relative deformation (flap amplitude) either. The latter observation is consistent with the data of Heathcote and Gursul, 2007 (see Figures 18a and 21a). Hence there is a suggestion of optimal deformation, whether it is absolute or relative with respect to the rigid foil.

In addition, the effect of the resonance frequency can be seen clearly. For the most flexible plate (shown with open diamond symbols and dashed line), the amplitude of the absolute deformation is becoming a maximum around $Sr_c \sim 0.8$, suggesting this is near the resonant frequency (see Fig. 5a). Hence, for all other flexible plates, the resonant frequency will be higher, and all data used in this article correspond to frequencies below the resonant frequency.

Figure 5 also shows the effect of the plunge amplitude. Both the absolute deformation amplitude and the flap angle amplitude are smaller for the larger plunging amplitude. This is due to the fact that, for the same Strouhal number based on the plunging amplitude, plunge frequency is smaller for the larger plunge amplitude. As a result, deformation is smaller, which produces less thrust.

We believe there is also a second reason for the ineffectiveness of large plunge amplitudes. This is the flow separation and vortex formation at the leading-edge, which becomes more dominant at large amplitudes. Even for the rigid foil in Figure 3c, the parabolic shape is no longer observed and a "kink" in the curve is present, which is due to the formation of the leading-edge vortex (see Cleaver et al. 2013).

The effect of deformation on the level of drag reduction is shown in Fig. 6. These contour plots encompass all data collected for L = 0.2c, 0.3c and 2c/3 and therefore encompass a wide range of Strouhal numbers, amplitudes and flexibilities. The data for the largest flexible part is extracted from Heathcote and Gursul (2007). The contours represent performance improvement, please note the changing scale with increasing L. Despite the very wide range of experimental parameters all three contour plots demonstrate an optimum in the region of $\lambda \approx 2$. In the case of Fig. 6c this is only suggested because the experimental measurements do not include low enough values of elastic parameter to clearly define the peak. Comparable values for *Bombus* and *Manduca* using the values of EI from Combes and Daniel (2003) and typical wing surface and forward flight speed from Shyy et al. (2008) are $\lambda \approx 2$ and $\lambda \approx 0.9$ respectively. This optimum elastic parameter correlates with optimal flap angle amplitudes: $\delta_{opt} = 7^0$ to 13^0 for L = 0.2c to 2c/3.

A very recent article (Lucas et al. 2014) suggests that a wide range of animals (bats, birds, insects, fish, cetaceans) employing chordwise and spanwise flexibility exhibit a narrow range of relative deformation angle with a mean value of 26.5 degrees and flexion ratio (effectively the length of the rigid section) with a mean value of 0.65. Although the nature has somewhat larger relative deformation angle than our optimal flap angle, this may be due to the simple plunging motion and smaller chordwise flexibility used in our experiments.

The effect of deformation on the time-averaged flow field is shown in the top row of Fig. 7. Here the foil shape at the extremes are shown schematically. For the rigid case there is a clear time-averaged jet in the wake of the airfoil implying thrust generation. For the optimal case the time-averaged jet is both broader and slightly stronger implying increased thrust. For the post-optimal case the time-averaged jet is weaker and narrower implying decreased thrust. The underlying reason for this variation in time-averaged jet strength is demonstrated in the phase-averaged vorticity contour plots shown in Fig. 7a to d. These figures show the phase-locked shape of the flexible section. The rigid case is shown in the left column, the optimal in the central column, and the post-optimal in the right column. For each case four phases are considered: top, middle (down), bottom, and middle (up). For all three cases the

flow fields are qualitatively similar, during the downward motion (Fig. 7a to c) a counter-clockwise TEV forms, and during the upward motion (Fig. 7c to a) its clockwise counterpart forms. These TEVs convect into the wake to form a reverse-Kármán vortex street which is responsible for the time-averaged jet. At the leading-edge a counter-clockwise LEV forms during the upward motion and convects along the lower surface gradually being dissipated such that at the tip of the flexible part it is so weak as to be no longer visible. Its inverse partner is visible above the airfoil in Figures 7b and c.

Quantitatively however the flow fields differ. The TEVs are visibly weaker in the post-optimal case than the optimal, and marginally weaker in the rigid case, this is quantified in Fig. 8. This figure demonstrates that optimal flexibility increases the strength of the TEVs, $\Gamma/U_\infty c$, enhancing the time-averaged jet and thereby increasing drag reduction. This is in agreement with the Kármán and Burgess equation (Von Kàrmàn and Burgess, 1935) for thrust due to a reverse-Kármán street. The effect is so strong as to give an almost linear dependency between mean TEV circulation and drag reduction. There was less difference in vortex spacing but this may just be a characteristic of the smaller lengths of the flexible plates.

An interesting question is why does the circulation decrease in the post-optimal regime and how does this relate to the optimal flap amplitude of $\delta_{opt} = 7^0$ to 13^0? A simple explanation may be flow separation at large flap angle amplitudes as described in the Introduction. Ramananarivo et al. (2011) suggest that the thrust becomes maximum when the slope angle at the trailing-edge equals the maximum effective angle of attack α_{eff} because this condition ($\delta/\alpha_{eff} \approx 1$) minimizes flow separation. The values for the optima shown in Figures 4b and 4c are: $\delta/\alpha_{eff} \approx 0.3$, and the optimal value for the results of Heathcote and Gursul (2007) is $\delta/\alpha_{eff} \approx 0.5$. This is a relatively wide range and rules out a direct correlation of optimal flap angle with δ/α_{eff}. It is likely that a simple explanation of optimal flap angle does not exist. If flow separation plays a role then both amplitude and phase of the flap angle should be important, and may explain the formation of weaker vortices in the post-optimal regime. This aspect remains unresolved.

4. Conclusions

The effect of flexibility on the time-averaged thrust can be beneficial for plunging foils even when the flexible region is confined to a small section near the trailing-edge. Short

thin plates attached to the foil have been tested for a wide range of flexibilities. The improvement was shown to be larger for smaller plunge amplitude and for longer flexible plates. The peak improvement was therefore 28% for the smallest amplitude and largest flexible plate. It was effective over a wide range of elastic parameter with optima in the region of $\lambda \approx 2$. This value of elastic parameter was related to an optimal value of flap angle amplitude of $\delta = 7^0$ to 13^0 for a wide range of lengths of flexible plate and plunge amplitude. It was hypothesized that these optima are due to the flow separation at large flap angles but no direct correlation of flap angle amplitude to effective angle of attack was found to support this hypothesis. While the role of flow separation remains unresolved, flow field measurements showed that the optimal case was closely related to strengthening of the trailing-edge vortices leading to a stronger time-averaged jet.

Acknowledgements

The authors would like to acknowledge the support from the Department of the Navy Grant N62909-10-1-7117 issued by the Office of Naval Research Global.

References

Cleaver, D.J., Wang, Z., and Gursul, I., 2012. Bifurcating flows of plunging airfoils at high Strouhal numbers. Journal of Fluid Mechanics, 708, 349-376.

Cleaver, D.J., Calderon, D.E., Wang, Z., Gursul, I., 2013. Periodically plunging foil near a free surface. Exp. Fluids 54, No. 3, 1491-1509.

Combes, S.A., Daniel, T.L., 2003. Flexural stiffness in insect wings I. Scaling and the influence of wing venation. J. Exp. Biology 206, No. 17, 2979-2987.

Dewey, P.A., Boschitsch, B.M., Moored, K.W., Stone, H.A., and Smits, A.J., 2013. Scaling laws for the thrust production of flexible pitching panels. Journal of Fluid Mechanics, 732, 29-46.

Frampton, K.D., Goldfarb, M., Monopoli, D., Cveticanin, D., 2002. Passive aeroelastic tailoring for optimal flapping wings, in: Fixed and Flapping Wing Aerodynamics for Micro Air Vehicle Applications. Amer Inst Aeronautics & Astronautics, Reston.

Gursul, I., Cleaver, D.J. and Wang, Z., 2013, "Control of low Reynolds number flows by means of fluid-structure interactions", Progress in Aerospace Sciences**,** http://dx.doi.org/10.1016/j.paerosci.2013.07.004

Heathcote, S., 2006. Flexible flapping airfoil propulsion at low Reynolds numbers, PhD Thesis, Dept of Mechanical Engineering. University of Bath, Bath, p. 167.

Heathcote, S., Gursul, I., 2007. Flexible flapping airfoil propulsion at low Reynolds numbers. AIAA J. 45, No. 5, 1066-1079.

Heathcote, S., Wang, Z., Gursul, I., 2008. Effect of spanwise flexibility on flapping wing propulsion. J. of Fluids and Structures 24, 183-199.

Kang, C.K., Aono, H., Cesnik, C.E.S., Shyy, W., 2011. Effects of flexibility on the aerodynamic performance of flapping wings. J. Fluid Mech. 689, 32-74.

Lucas, K.N., Johnson, N.,beaulieu, W.T., Cathcart, E., Tirrell, G., Colin, S.P., Gemmel, B.J., Dabiri, J.O., and Costello, J.H., 2014. Bending rules for animal propulsion. Nature Communications, 5:3293 doi: 10.1038/ncomms4293.

Miao, J.M., Ho, M.H., 2006. Effect of flexure on aerodynamic propulsive efficiency of flapping flexible airfoil. Journal of Fluids and Structures 22, No. 3, 401-419.

Michelin, S. and Smith, S.G.L., 2009. Resonance and propulsion performance of a heaving flexible wing. Physics of Fluids 21, No. 7, 071902.

Michell, J.H., 1893. The highest waves in water. Philosophical Magazine Series 5 36, 430-437.

Moffat, R.J., 1988. Describing the uncertainties in experimental results. Exp. Therm. Fluid Sci. 1, No. 1, 3-17.

Palm, E., Grue, J., 1999. On the wave field due to a moving body performing oscillations in the vicinity of the critical frequency. J. Eng. Math. 35, No. 1-2, 219-232.

Pierson, W.J., Moskowitz, L., 1964. A proposed spectral form for fully developed wind seas based on the similarity theory of S. A. Kitaigorodskii. Journal of Geophysical Research 69, No. 24, 5181-5190.

Ramananarivo, S., Godoy Diana, R., Thiria, B., 2011. Rather than resonance, flapping wing flyers may play on aerodynamics to improve performance. Proceedings of the National Academy of Sciences of the United States of America 108, No. 15, 5964-5969.

Shyy, W., Lian, Y.S., Tiang, J., Viieru, D., Liu, D., 2008. Aerodynamics of low Reynolds number flyers. Cambridge University Press.

Tsuji, Y., Nagata, Y., 1973. Stokes' expansion of internal deep water waves to the fifth order. Journal of Oceanography 29, No. 2, 61-69.

Von Kàrmàn, T., Burgess, J.M., 1935. General Aerodynamic Theory - Perfect Fluids, in: Aerodynamic Theory. Springer, Berlin.

Zhu, Q., Liu, Y., Yue, D., 2006. Dynamics of a three-dimensional oscillating foil near the free surface. AIAA J. 44, No. 12, 2997-3009.

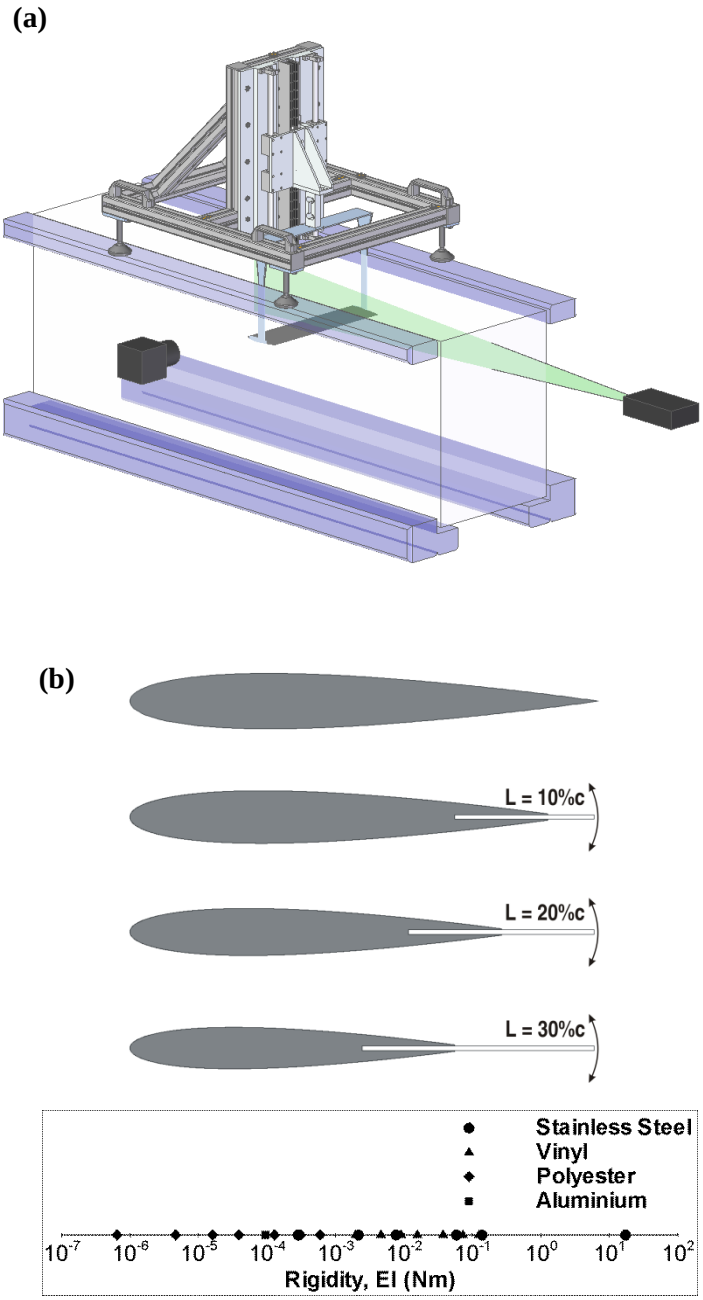

Fig. 1 a) Test section with PIV equipment and experimental rig, and b) flexible trailing-edge design. Inset shows the range of possible rigidities achieved through the use of 21 combinations of material and thickness.

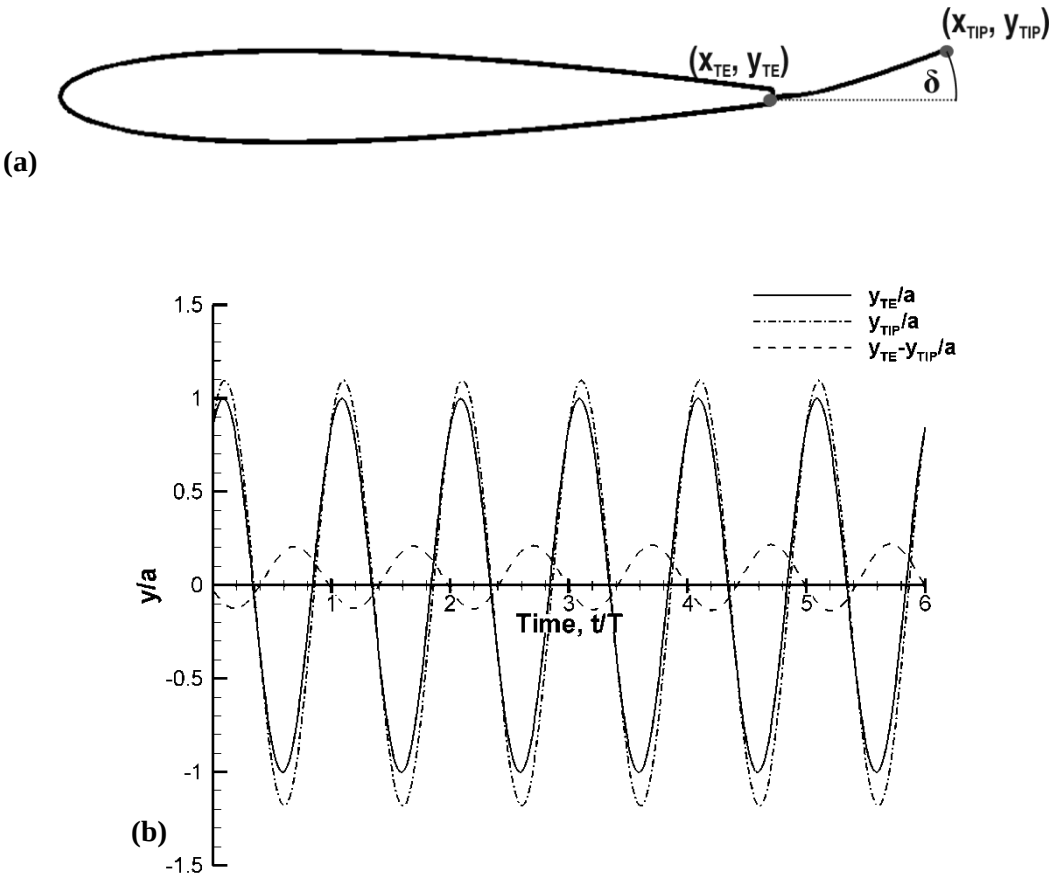

Fig. 2 Deformation measurements: a) coordinates used for motion tracking, b) typical sinusoidal curve fit to the trailing-edge and tip measurements, and associated deformation.

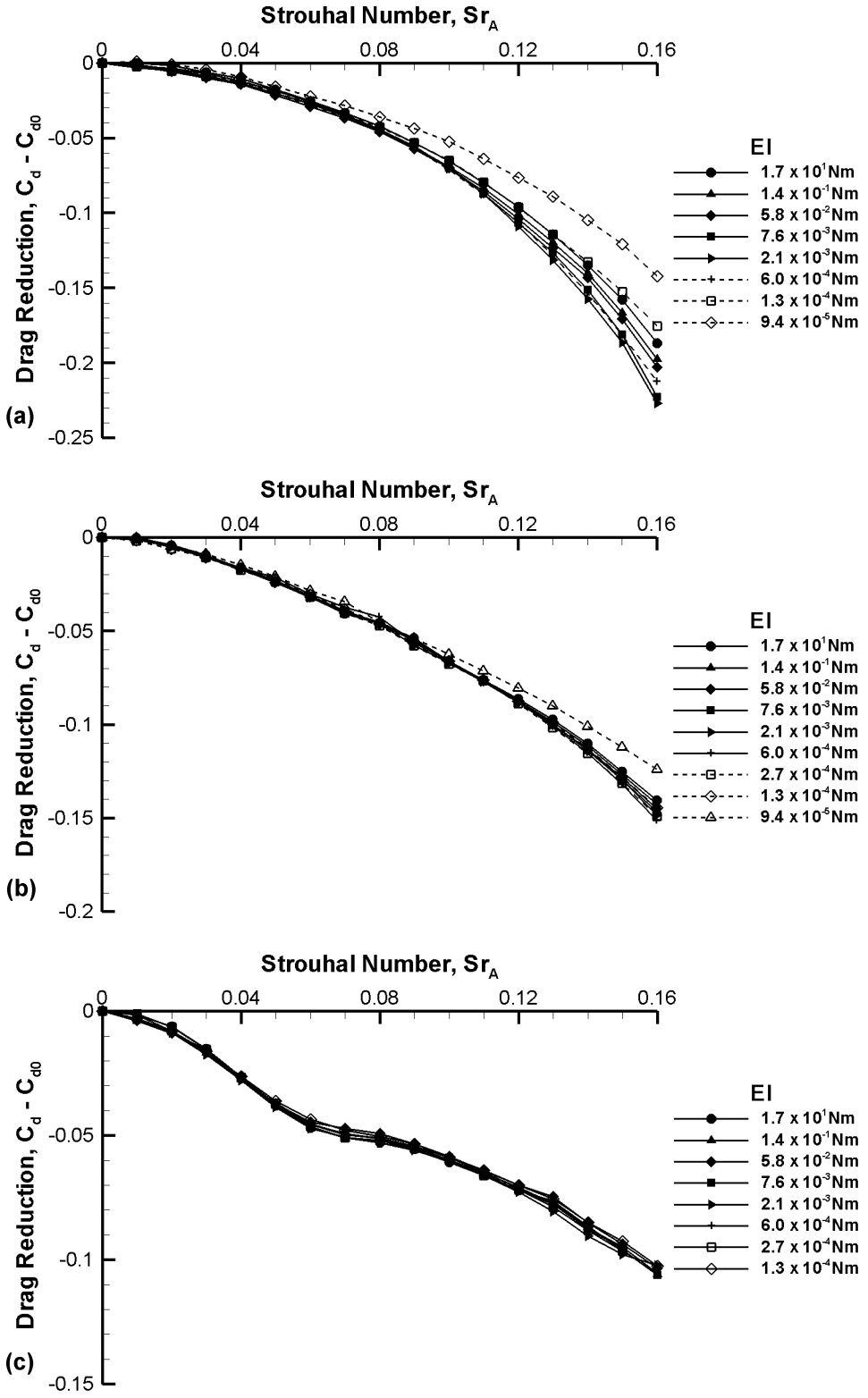

Fig. 3 Reduction in time-averaged drag coefficient against Strouhal number based on amplitude for a foil with a flexible portion (rigidity shown in legend) of length $L = 0.2c$ oscillated with amplitudes of: a) a/c = 0.1, b) a/c = 0.2, and c) a/c = 0.5.

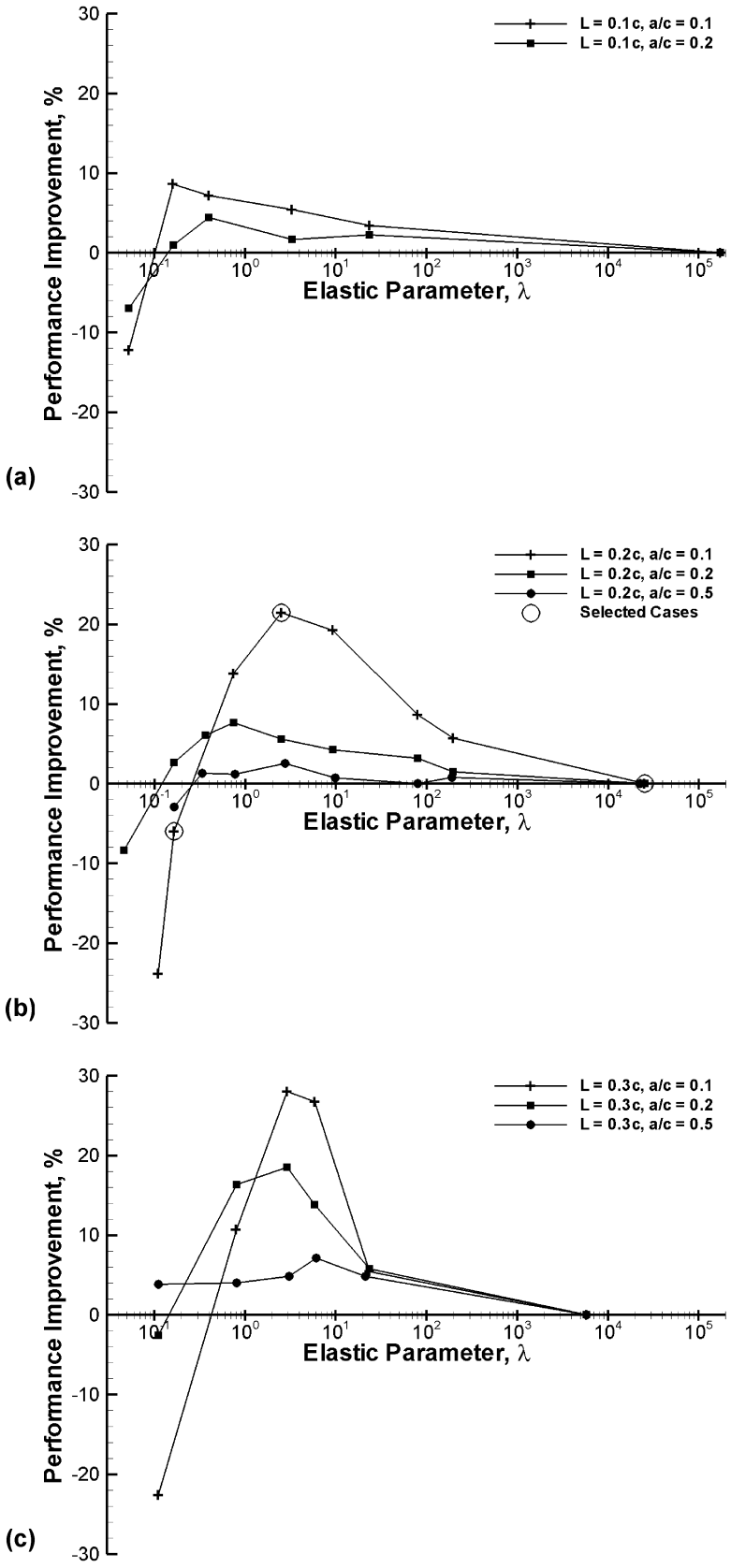

Fig. 4 Improvement in drag reduction due to flexibility at the maximum Strouhal number tested for: a) L = 0.1c, b) L = 0.2c, and c) L = 0.3c. Highlighted rigid, optimal, and post-optimal points in b) are used in Figures 7 and 8.

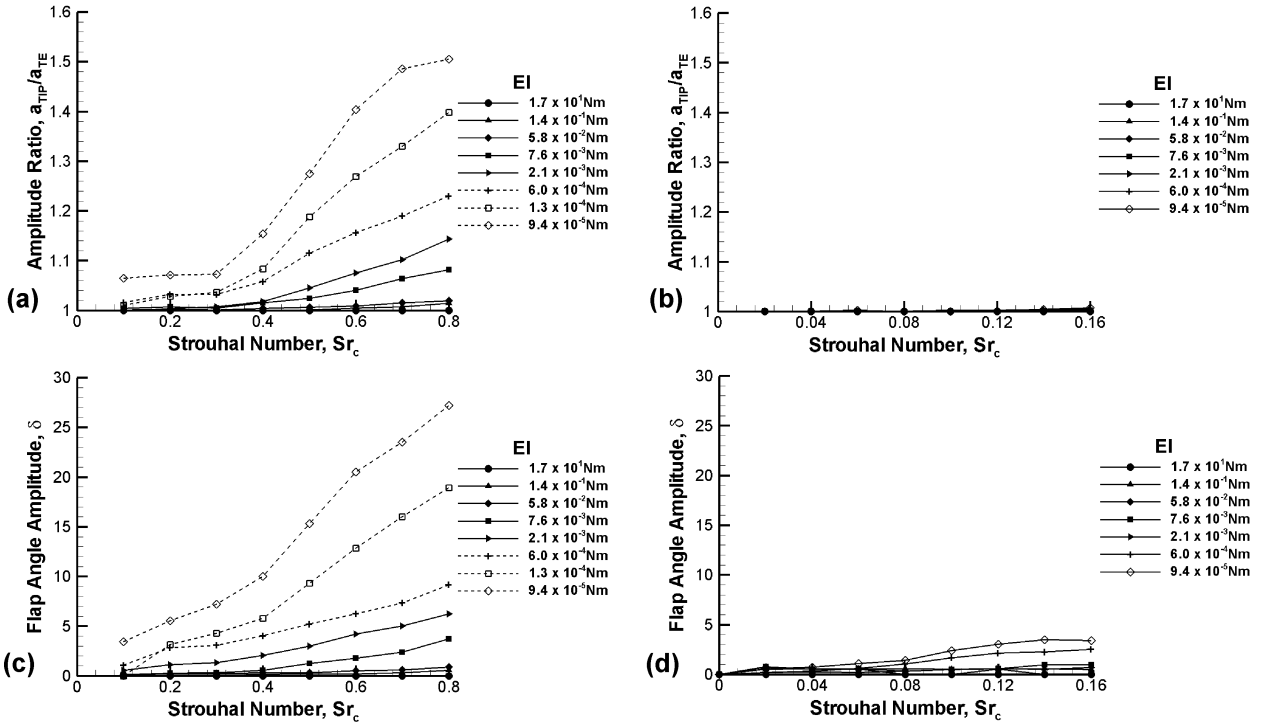

Fig. 5 – a, b) Amplitude ratio, and c, d) flap angle amplitude against Strouhal number based on chord for $a = 0.1c$ (left column) and $a = 0.5c$ (right column) for $L = 0.2c$.

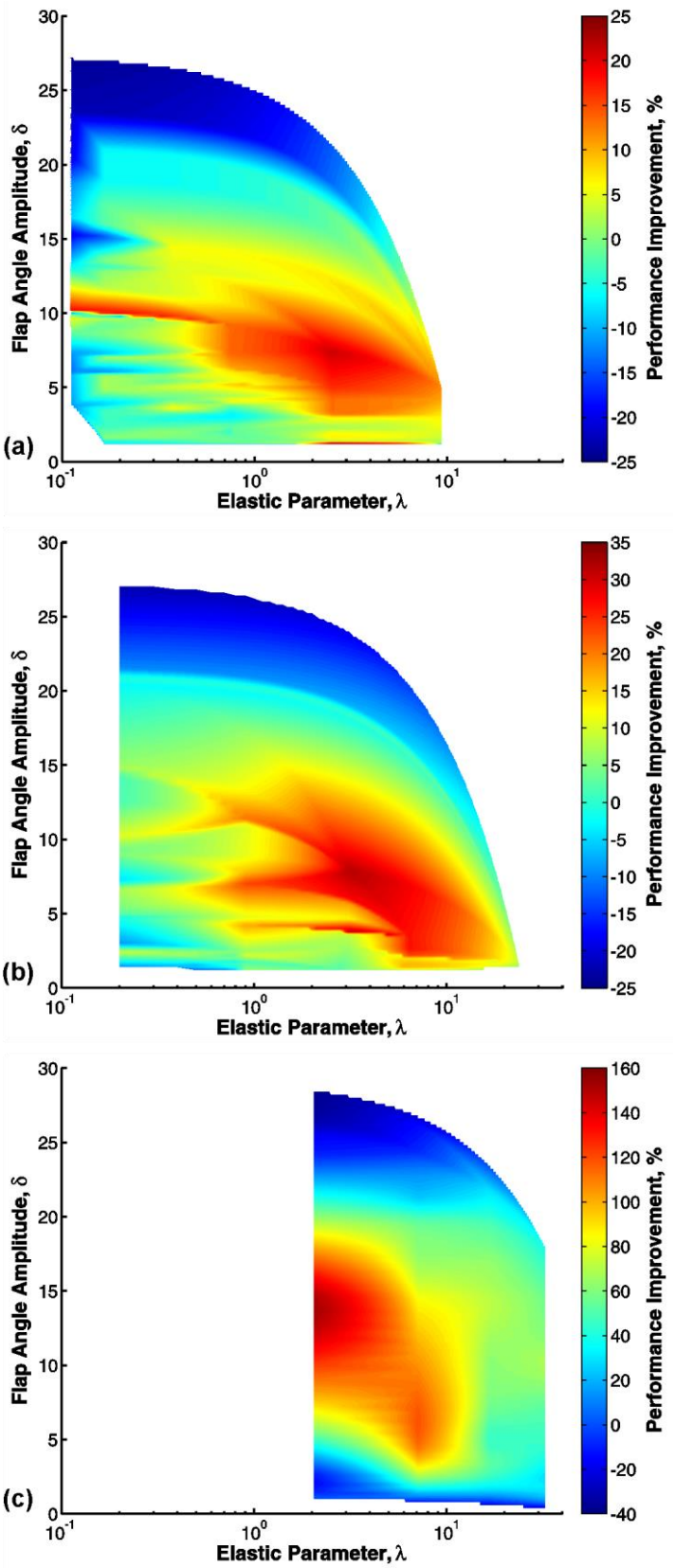

Fig. 6 Contour plots of performance improvement in the elastic parameter versus flap angle amplitude parameter space for all amplitudes, Strouhal numbers and: a) $L = 0.2c$, b) $L = 0.3c$ and c) $L = 2c/3$ from Heathcote and Gursul (2007).

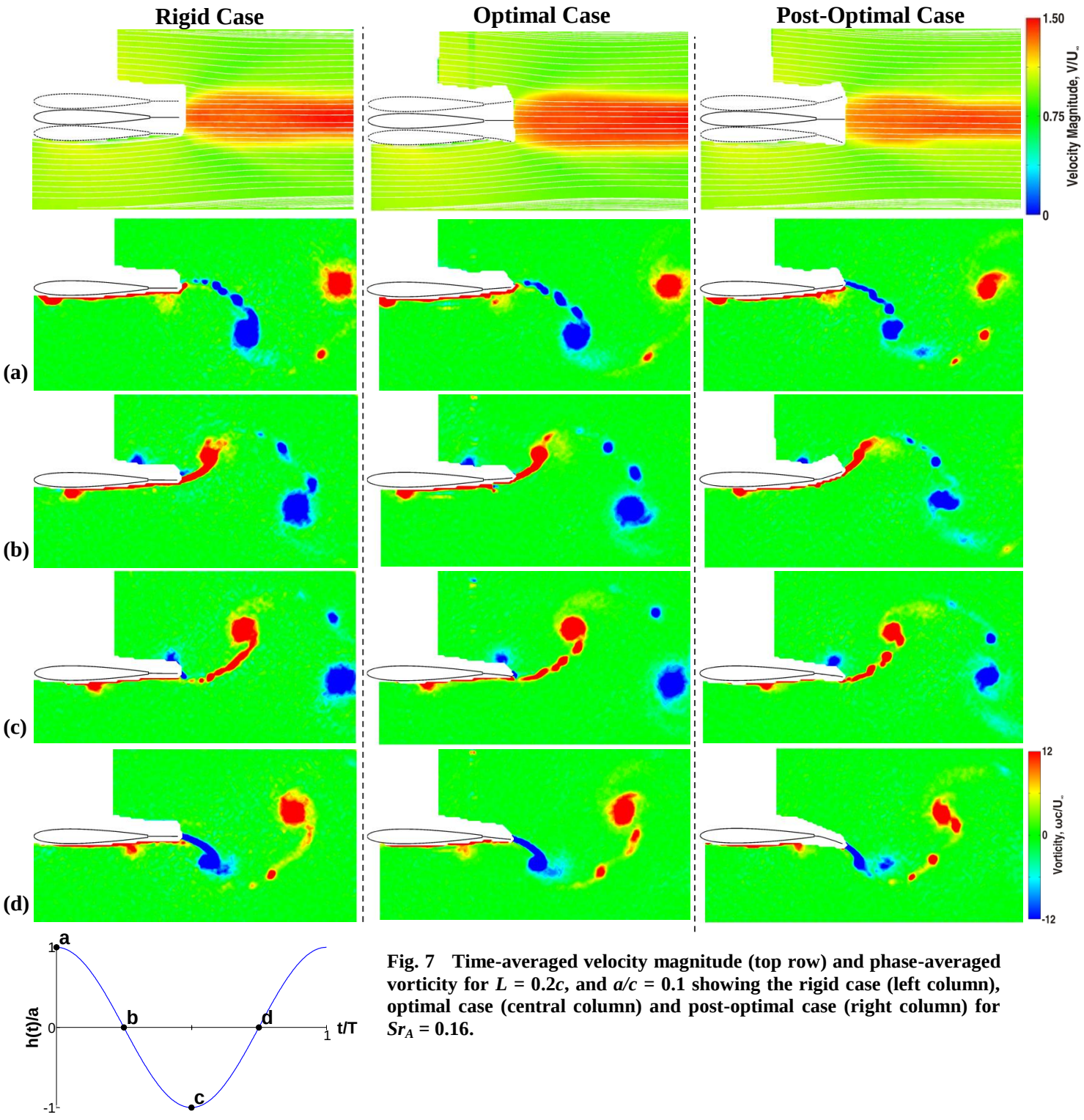

Fig. 7 Time-averaged velocity magnitude (top row) and phase-averaged vorticity for $L = 0.2c$, and $a/c = 0.1$ showing the rigid case (left column), optimal case (central column) and post-optimal case (right column) for $Sr_A = 0.16$.

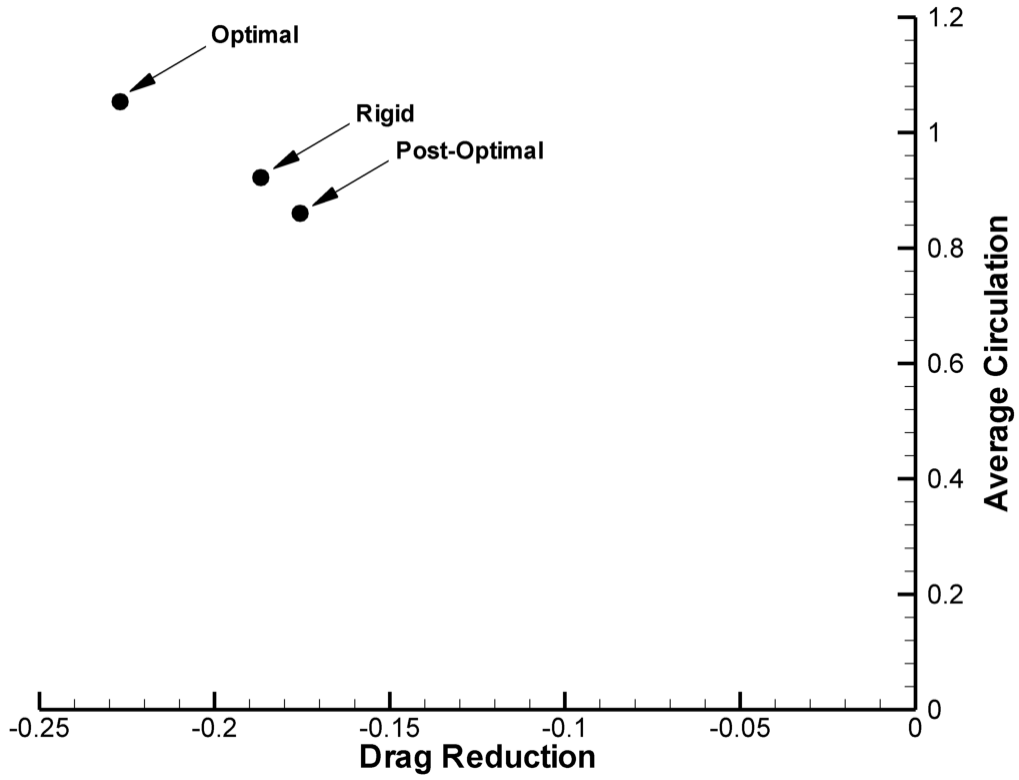

Fig. 8 Average normalized circulation of clockwise and counter-clockwise trailing-edge vortices versus reduction in the drag coefficient.